# Coupled discrete/continuum simulations of the impact of granular slugs with clamped beams: Stand-off effects

A. Goel[a], T. Uth[a], T. Liu[b], H.N.G. Wadley[c] and V.S. Deshpande[a*]

[a] *Department of Engineering, University of Cambridge,*
*Trumpington Street, Cambridge CB2 1PZ, UK*

[b] *Faculty of Engineering, University of Nottingham,*
*University Park, Nottingham NG7 2RD, UK*

[c] *Department of Material Science & Engineering, School of Engineering and Applied Science,*
*University of Virginia, Charlottesville, VA 22904, USA*

## Abstract

Coupled discrete particle/continuum simulations of the normal (zero obliquity) impact of granular slugs against the centre of deformable, end-clamped beams are reported. The simulations analyse the experiments of Uth et al. (2015) enabling a detailed interpretation of their observations of temporal evolution of granular slug and a strong stand-off distance dependence of the structural response. The high velocity granular slug generated by the pushing action of a piston develops a spatial velocity gradient due to stored elastic energy during the loading phase by the piston. The velocity gradient within the "stretching" slug is a strong function of the inter-particle contact stiffness and the time the piston takes to ramp up to its final velocity. Other inter-particle contact properties such as damping and friction are shown to have negligible effect on the evolution of the granular slug. The velocity gradients result in a slug density that decreases with increasing stand-off distance, and therefore the pressure imposed by the slug on the beams is reduced with increasing stand-off. This results in the stand-off dependence of the beam's deflection observed by Uth et al. (2015). The coupled simulations capture both the permanent deflections of the beams and their dynamic deformation modes with a high degree of fidelity. These simulations shed new light on the standoff effect observed during the loading of structures by shallow buried explosions.

*Keywords:* Granular material; Particle impact; Discrete particle simulation; Fluid-structure interaction; Landmine; Blast.

*Corresponding author. E-mail address: vsd@eng.cam.ac.uk .

# 1.    Introduction

Much attention has been devoted to the dynamic response of above-ground structures subjected to blast loading from a shallow-buried explosion (Anderson et al., 2011). Experimental as well as numerical studies have shown that compared to surface laid explosives, shallow-buried explosives result in higher impulse transmission and larger deflections of the afflicted structure (Deshpande et al., 2009; Peles et al., 2008; Pickering et al., 2012). This increased severity of loading has been attributed to the impact of the granular media that is ejected by the expansion of detonation products in shallow buried explosives (Bergeron and Tremblay, 2000; Fairlie and Bergeron, 2002; Reichenbach et al., 1991) compared to explosions in air.

A number of experimental studies have proposed empirical relations to quantify the deformations of plates subjected to buried explosions; see for example Westine et al. (1985) and Neuberger et al. (2007). Based on such empirical relations, Morris (1993) proposed a design-for-survivability code for structures subjected to such impulsive loading events. A parallel effort has sought to numerically simulate the deformations of structures subjected to the complex loadings created by such explosions. For example, Rimoli et al. (2011) used a soil model (Deshpande et al., 2009) to deduce the impulse applied to structures by explosively driven spherical sand, and then simulated the ensuing (uncoupled) deformation of aluminium monolithic and sandwich plates using finite element calculations. Gruijicic et al. (2008a, 2008b, 2006) and Wang et al. (2004) have presented coupled Eulerian/Lagrangian simulations of landmine explosions and attempted to compare their predictions with blast impulse and plate deformation measurements from Bergeron and Temblay (2000) and Foedinger (2005).

More recently, coupled discrete particle/continuum simulations have been used to investigate the response of structures impacted by high velocity granular media. For example, Borvik et al. (2011) followed by Dharmesena et al. (2013), and Holloman et al. (2015a, 2015b) used this approach to simulate the response of a variety of monolithic and sandwich structures loaded by high velocity sand sprays generated by the buried explosions. Various calibrated parameters are used to produce the high velocity sand spray generated by the expanding explosive and the measurements of the response of the structure impacted by this spray are compared against the predictions. In all cases, discrepancies exist between measurements and predictions. One issue arises from the ill-defined foundation upon which a buried explosive rests. With the use of concentric soil shells surrounding suspended explosive charges, Wadley et al. (2013) has overcome this issue, discrepancies still remain. The origin of these discrepancies remains unresolved with possible sources of error being:

(i)    Inability of the simulations to accurately capture the details of the granular spray generated by the loading of the soil due to the expansion of the explosive gas; and/or

(ii)    Failure of the simulations to correctly capture the interactions between the high velocity granular ejecta and the impacted structure.

The decoupling of these two possible sources of error is problematic in experiments involving detonation of an explosive since (i) typically spherically expanding, optically opaque sand sprays are generated (Hlady, 2004; Pickering et al., 2012; Dharmesena et al., 2013) wherein only the outer front is visible and (ii) the explosive gases obscure the view of the impacted structure after the first few milliseconds.

Therefore, the only metric available to compare simulations and measurements is the permanent deformations of the structures. This metric is an integrated (and therefore very coarse) measure of the fidelity of the simulations and makes it difficult to determine the precise sources of any discrepancies.

In order to address this deficiency, Park et al. (2013) developed a technique to generate a high-velocity sand slug within a laboratory setting and without the need for the detonation of an explosive. Uth and Deshpande (2014) and Uth et al. (2015) employed this setup to investigate the dynamic response of monolithic and sandwich structures impacted by such granular slugs. The key feature of these experiments was that the high velocity granular slugs were fully characterised both the terms of their density and velocity spatial distributions. Moreover, Uth and Deshpande (2014) and Uth et al. (2015) reported detailed observations of the dynamic response of the impacted structures visualised using high-speed photography.

Pingle et al. (2012) have analysed the interaction of spatially uniform granular slugs impacting rigid targets. This rather idealised, but fundamental fluid-structure interaction (FSI) problem is the "sand-blast" analogue to the classical water propagated shock FSI problem studied by Taylor (1963). Liu et al. (2013) extended the sand column model to investigate the impact of clamped sandwich and monolithic plates. Their numerical results indicate that some edge clamped sandwich panel designs suffer significantly smaller deflections than monolithic plates of identical span and of equal mass per unit area. The performance benefit was due to the higher bending strength of sandwich plates. This contrasts with water-blast of sandwich structures, where significant benefits accrue from fluid-structure interaction effects (Deshpande and Fleck, 2005; Dharmasena et al., 2010; Wadley et al., 2008; Wei et al., 2007). The loading of structures by a slug of high velocity granular particles not only provides physical insight into the interaction of granular media with structures, but is also directly representative of the ejecta created during a shallow buried explosion as shown in the landmine explosion experiments reported by Joynt and Williams (private communication), Holloman et al. (2015a, 2015b) and Park et al. (2013). Thus, the impact of high velocity granular slugs against a test structure is of considerable theoretical and experimental interest.

Uth et al. (2015) reported experimental observations for the zero obliquity (normal) impact of granular slugs comprising tungsten carbide particles against clamped beams. These measurements provide extensive data that show the dependence of the dynamic response of the beams to not only the velocity of the slug but also the stand-off distance between the launch position of the slug and the location of the beam. While this data presented clear trends, a lack of numerical simulations precluded elucidation of the physical mechanisms at play in the experiments. In this study we report detailed numerical simulations of the experiments of Uth et al. (2015). Comparisons with the experiments are used to (i) provide a detailed test of the fidelity of the coupled discrete particle/continuum simulation methodology and (ii) provide mechanistic explanations for the temporal evolution of the granular slugs and the ensuing stand-off dependence of the beam dynamic responses observed in the experiments.

## 2.    Summary of experimental findings

Uth et al. (2015) presented an experimental investigation of the response of monolithic beams impacted normally and centrally by slugs of Tungsten Carbide (WC) particles. Here we analyse the data from Uth et al. (2015) to test the fidelity of the coupled discrete particle/continuum numerical models[1]. It is thus instructive to first briefly describe the experimental set-up and the key findings.

Cylindrical slugs of mass 22.7g (diameter $D_0 = 12.7$ mm and resting length $L_0 = 20$ mm), comprising WC particles with a diameter range of 45-150 µm were impacted against monolithic clamped AISI 304 stainless steel beams. A sketch of the experimental setup is included in Fig. 1 and comprises four main components (from right to left): (i) a gas gun to fire a solid projectile, which then accelerates the piston of (ii) a slug launcher apparatus based upon that developed by Park et al. (2013); (iii) a WC slug that initially rests inside the cylindrical cavity of the launcher; and (iv) the beams clamped to a support rig. The projectile fired from the gas gun impacts the piston which in turn pushes the granular slug within the cylindrical cavity towards the clamped beam. The impact velocity of the projectile sets the speed with which the slug impacts the beam centre at normal incidence angle.

Clamped 304 stainless steel beams of span $L = 100$ mm, width 21.3 mm and thickness 0.69 mm were used in the experiments of Uth et al. (2015). High speed photography was employed in the experiments to visualise both the granular slug in free-flight and the subsequent impact of the slug against the beam as well as the ensuing deformations.
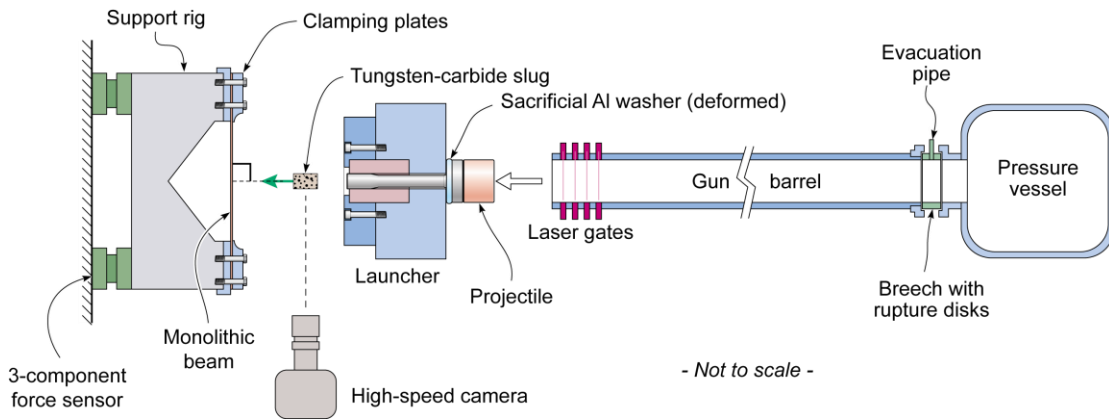


Figure 1: Sketch of the experimental setup used in the experimental investigation of Uth et al. (2015) to investigate the impact of granular slugs comprising WC particles against clamped beams.

### 2.1    Key experimental measurements

Uth et al. (2015) presented their data in terms of the projectile impact velocity $V_0$ and the average velocity of the granular slug. However, for the purposes of the numerical calculations presented here it is more convenient to present the results in terms of

---

[1] We emphasize that while the data from the study of Uth et al. (2015) used here was gathered in the original investigation, we reanalyzed some of their data (especially the high-speed photographs) in order to extract some additional information (e.g. the velocity of the piston) required for the numerical calculations.

piston velocity $v_p$: details of the method employed to determine $v_p$ from the measurements are presented in Section 4.2.

The evolution of the granular slug ejected by a piston velocity $v_p = 83.5 \text{ m s}^{-1}$ as visualised by high speed photography is shown in Fig. 2a. Images at four instants in time are shown with time $t_s = 0$ chosen arbitrarily for the first snapshot corresponded to the time at which the distance $s$ travelled by the slug was $s = 51$ mm. The travel distance $s$ is defined in Fig. 2b which shows the launcher section of the apparatus: $s$ is equal to the distance travelled by the leading edge of the granular slug from its resting position within the launcher. The images clearly show that while the slug remains approximately cylindrical with an invariant diameter, it lengthens with increasing $s$. This is emphasised in Fig. 2c where the evolution of the slug length $L_s$ ($L_s = L_0$ at $s = 0$) is shown as a function of $s$ for two piston velocities.
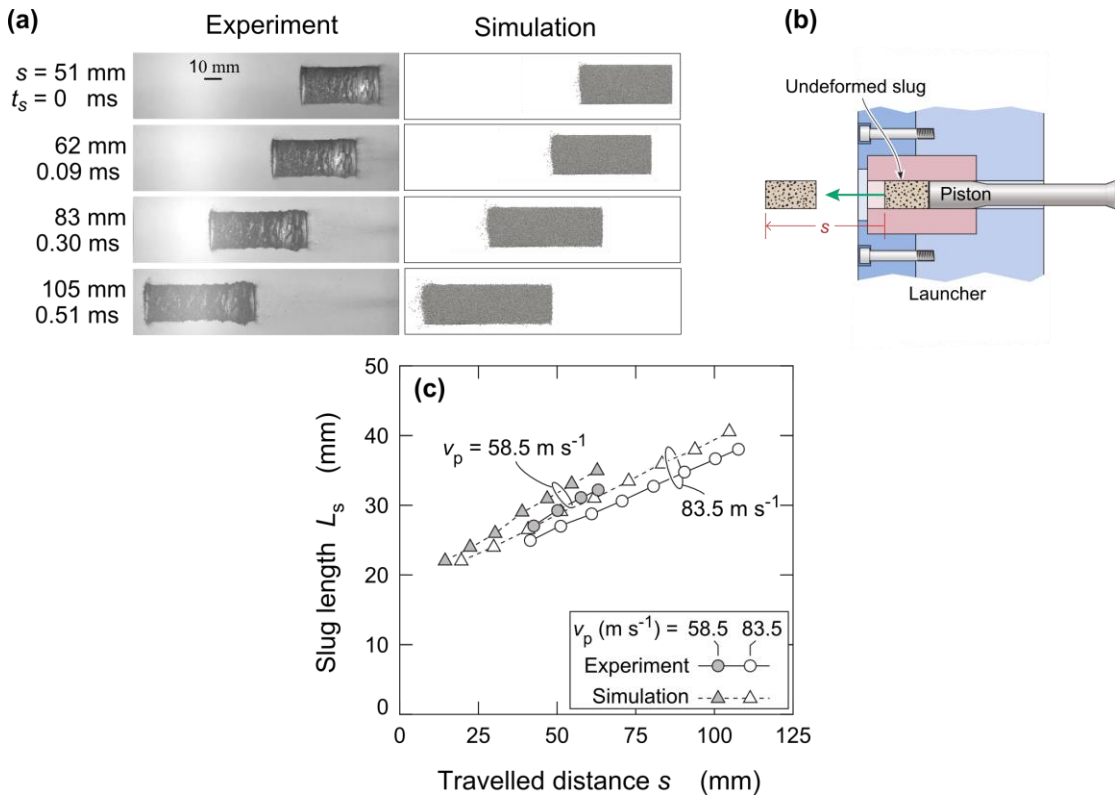


Figure 2: (a) Snapshots from the observations of Uth et al. (2015) and corresponding simulations showing the evolution of the granular slug generated (by piston velocity $v_p = 83.5 \text{ m s}^{-1}$) at four selected values of the distance travelled $s$. The distance $s$ is defined in (b) while time $t_s = 0$ is chosen arbitrarily for the first snapshot. (c) The corresponding measurements and predictions of the variation of the slug length $L_s$ with $s$ for two selected values of $v_p$.

High speed photographs of the impact of the granular slug against the clamped beam located at a standoff $S = 65$ mm are shown in Fig. 3a for $v_p = 69.5 \text{ m s}^{-1}$. Here the standoff $S$ is defined in Fig. 4 and is equal to the distance between the leading end of the resting granular slug within the launcher and the front face of the beam. Upon impact, a plastic travelling hinge emanates from the impact site and travels to the supports. Simultaneously, the slug compacts and flows against the beam as it deforms

(Fig. 3a). The permanent deflections $w_p$ of the beam mid-span (i.e. residual deflection at time $t \to \infty$ after impact) are plotted in Fig. 5 as a function of $v_p$ for two values of the standoff $S$: the deflections increase with increasing $v_p$ and decreasing $S$. These are the primary observations that we aim to model and thereby provide a more physical understanding of the mechanisms involved in interaction of high velocity granular media with deformable structures.
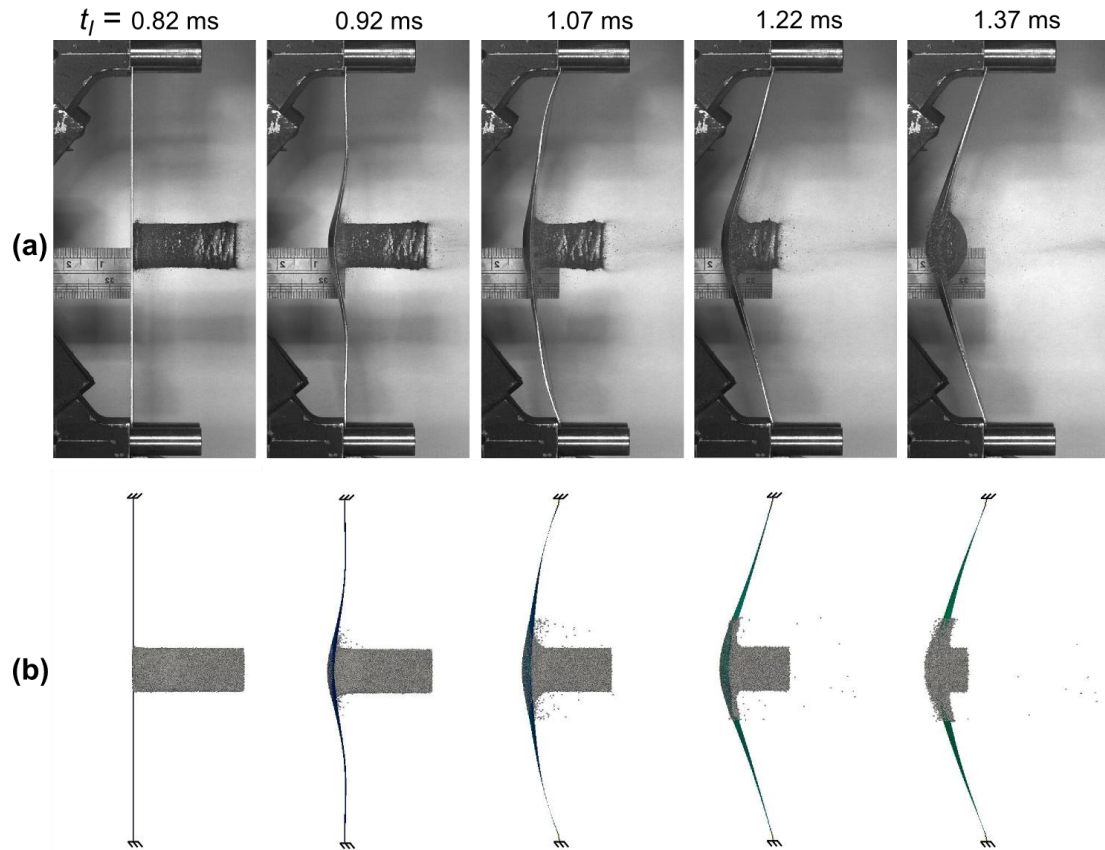


Figure 3: (a) High speed photographs showing a side view a granular slug generated by a piston at $v_p = 69.5 \text{ m s}^{-1}$ impacting the clamped beam at a stand-off $S = 65$ mm (Uth et al., 2015). Photographs are shown at 5 selected values of time $t_I$, where $t_I = 0$ corresponds to the instant the projectile impacts the piston. (b) The corresponding predictions using the coupled discrete/continuum simulations are also included.
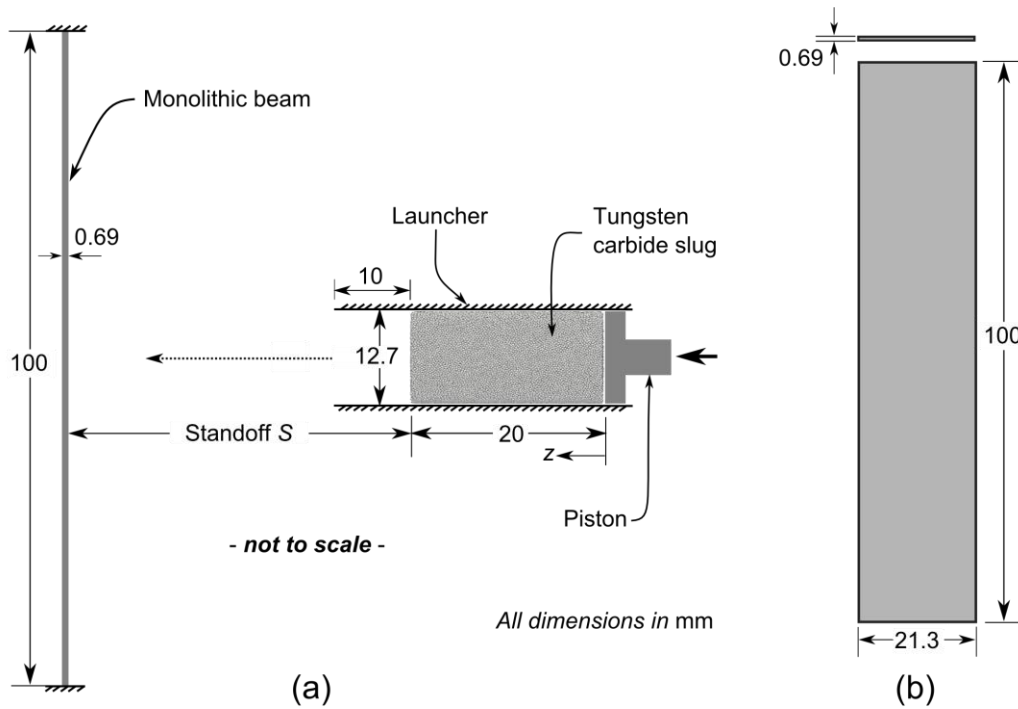
Figure 4: (a) A side view sketch showing the setup used in the numerical simulations of the experiments of Uth et al. (2015) and (b) plan view of the beam to show the span and width. All critical dimensions of the launcher, granular slug and beam are marked along with the definition of the stand-off $S$. The sketch is not shown to scale.
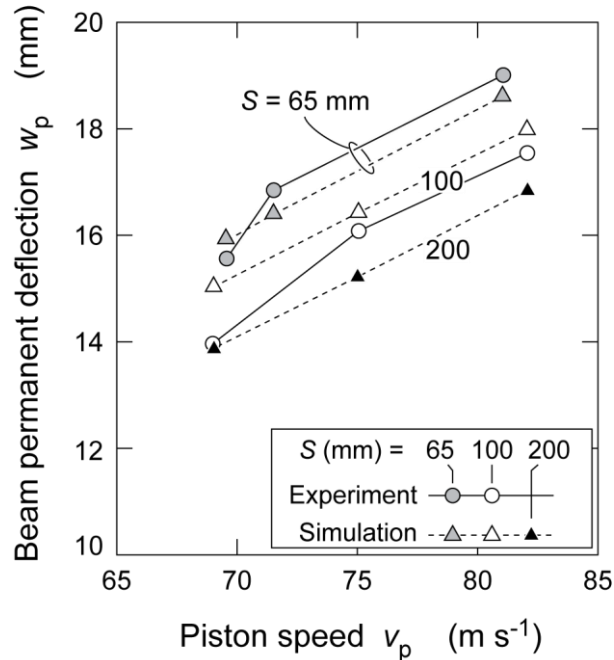


Figure 5: Comparison between measurements and predictions of the permanent deflection of the mid-span of the beam as function of the piston velocity $v_p$. The results are shown for the two values of stand-off $S = 65$ mm and $110$ mm investigated by Uth et al. (2015). In addition predictions for $S = 200$ mm are also included.

## 3. Numerical simulation methodology

The deformation of the beams resulting from impact of the WC particles was modelled using a coupled discrete particle/Lagrangian finite element simulation scheme. In this approach the WC particles were modelled as discrete spherical particles using the GRANULAR package in the multi-purpose molecular dynamics code LAMMPS[2] while the beams were modelled within the Lagrangian commercial finite element package Abaqus[3]. These two modelling schemes were coupled using the multi-physics coupling code interface (MpCCI[4]) interface as described below. The modelling scheme therefore consisted of four steps: (i) the discrete particle approach to model the WC particles; (ii) generation of the high velocity slug due to the pushing of the slug out of the launcher by the piston; (iii) an FE scheme to model the beam; (iv) an MpCCI interface for coupling between the discrete particle and FE schemes. Effects of gravity and air drag[5] are neglected in the simulations.

### 3.1 Discrete particle calculations

The discrete particle calculations are done using the GRANULAR package in the multi-purpose molecular dynamics code LAMMPS (Plimpton, 1995). Three dimensional simulations are performed using mono-sized spherical particles of diameter $D$ and mass $m_p$. The granular package in LAMMPS is based on soft-particle contact model (Fig. 6), introduced by Cundall and Strack (1979) and extended to large scale simulations by Campbell and Brennen (1985) and Campbell (2002). The contact law comprises:

(i)　　Linear spring with spring constant $K_n$ and linear dashpot with damping constant $\gamma_n$ connected in parallel, governing the contact in the direction connecting the particle centres.

(ii)　　Linear spring of constant $K_s$ and Coulomb friction coefficient $\mu$ connected in series, governing the tangential contact.
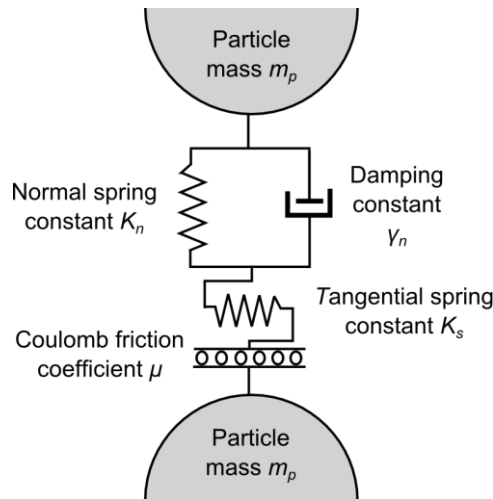


Figure 6: Sketch of the inter-particle contact model between spherical particles of diameter $D$ used to simulate the WC particles in the granular slug.

---

[2] LAMMPS: http:// lammps.sandia.gov/

[3] Abaqus: http://www.3ds.com/

[4] MPCCI: http://www.mpcci.de/

[5] At the relatively low velocities considered here, we are in a Stokes drag regime where the reduction in the velocity of the particles over the millisecond time frames considered are negligible.

With $r$ as the separation of the particle centres, and the interpenetration given by $\delta_n = r - D$, the normal force during active contact ($\delta_n < 0$) is given by

$$F_n = K_n \delta_n + m_{\text{eff}} \gamma_n \dot{\delta}_n, \tag{3.1}$$

where $m_{\text{eff}}$ is the effective or reduced mass of the two contacting bodies. We take $m_{\text{eff}} = m_p/2$ for impacts between particles, and $m_{\text{eff}} = m_p$ for impacts between a particle and the beam.

The tangential force $F_s$ only exists during active contact, and opposes sliding. It is limited in magnitude to $|F_s| < \mu|F_n|$ as follows. Define $\dot{\delta}_s$ as the tangential displacement rate between the contacting particles. Then, $F_s$ is given by an "elastic-plastic" relation of Coulomb type with stiffness $K_s$, i.e.

$$\dot{F}_s = \begin{cases} K_s \dot{\delta}_s & \text{if } |F_s| < \mu|F_n| \text{ or } F_s \dot{\delta}_s < 0 \\ 0 & \text{otherwise.} \end{cases} \tag{3.2}$$

The value of damping constant $\gamma_n$ dictates the loss of energy during normal collision and is directly related to the coefficient of restitution $e$ according to

$$e = \exp\left[-\pi\left(\frac{8\,K_n}{\gamma_n^2\,m_p} - 1\right)^{-1/2}\right]. \tag{3.3}$$

The collision time $t_e$ for individual binary collisions follows from (3.1) as

$$t_e = -2\,\frac{\ln(e)}{\gamma_n}, \tag{3.4}$$

and thus, in the limit of plastic collisions with $e \to 0$, the contact time $t_e \to \infty$.

Newton equations for both the translational and rotational motions of the particles were integrated using a Verlet time-integration scheme (i.e. Newmark-Beta with $\beta = 0.5$). The time-step for integration was taken to be less than $t_e/10$ in order to ensure accurate integration of the contact Eqs. (3.1) and (3.2).

*3.2    Finite element calculations & coupling to the discrete particle calculations*
The beams were modelled using three-node triangular elements (S3 in Abaqus notation). Clamped boundary conditions, with vanishing displacements were prescribed at the clamped ends (Fig. 4). The coupling between the LAMMPS discrete particle and the Abaqus finite element calculations was carried out via the MpCCI Code adapter API as follows. At any time $t$, suppose that a proportion of the particles are in contact with the plate. Consider one such particle. The displacement $\delta_n$ is defined as $\delta_n = r - D/2$, where $r$ is the distance between particle centre and contact point on the beam. The rate $\dot{\delta}_n$ is the relative approach velocity of the particle and the point of contact on the beam surface, and likewise $\dot{\delta}_s$ is the tangential velocity. The normal and tangential contact forces are calculated using Eqs. (3.1) and (3.2). These forces were then added as nodal forces to the appropriate elements of the Abaqus finite element calculations to complete the coupling between the discrete and finite element calculations.

### 3.3 Material properties

The beams were made from 304 stainless steel sheets which was modelled as J2-flow theory rate dependent solid of density $\rho = 7900 \text{ kg m}^{-3}$, Young's modulus $E = 210$ GPa and Poisson ratio $v = 0.3$. Uth et al. (2015) reported the quasi-static tensile stress versus strain curve for the 304 stainless they employed in their study measured at an applied plastic strain rate $\dot{\varepsilon}^p = 10^{-4} \, s^{-1}$. The response $\sigma_d(\varepsilon^p, \dot{\varepsilon}^p)$ at high strain rates $\dot{\varepsilon}^p$ is estimated as

$$\sigma_d(\varepsilon^p, \dot{\varepsilon}^p) = R(\dot{\varepsilon}^p)\sigma_0(\varepsilon^p), \tag{3.5}$$

where $\sigma_0(\varepsilon^p)$ is the measured quasi-static stress versus strain curve and $R(\dot{\varepsilon}^p)$ the strength enhancement at high rates that is extracted from the measurements by Lichtenfeld et al. (2006). The uniaxial tensile true stress versus equivalent plastic strain curves at plastic strain-rates $10^{-4} \, s^{-1} \leq \dot{\varepsilon}^p \leq 10^4 \, s^{-1}$ were tabulated in Abaqus using this prescription. Some selected curves are plotted in Fig. 7 including the quasi-static ($\dot{\varepsilon}^p = 10^{-4} \, s^{-1}$) curve from Uth et al. (2015) in order to illustrate the properties of the 304 stainless steel used in the FE calculations.
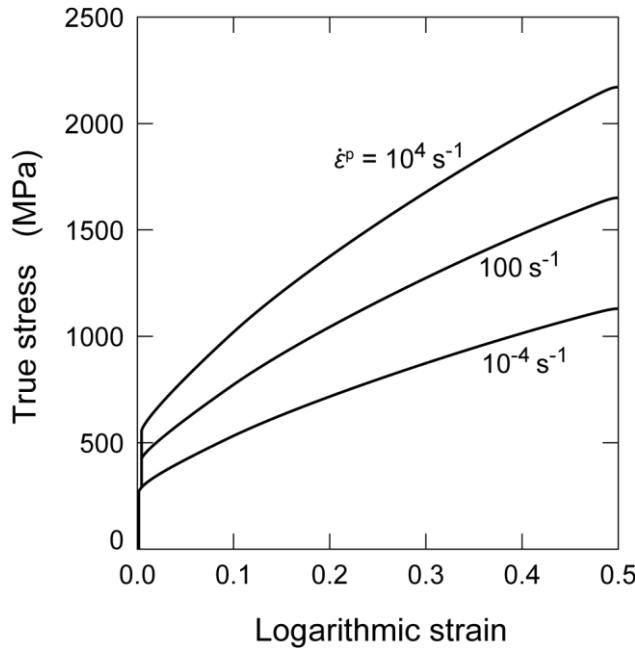


Figure 7: The uniaxial true stress versus logarithmic strain curves of the AISI 304 stainless steel used to manufacture the test beams. The data for the quasi-static response measured at a strain rate $\dot{\varepsilon}^p = 10^{-4} \, s^{-1}$ is from Uth et al. (2015) while the high strain rate behaviour is inferred from the measurements by Lichtenfeld et al. (2006) using Eq. (3.5).

The granular slug was modelled as comprising spherical particles of diameter $D = 300 \, \mu m$ made from a solid of density 15,630 kg m$^{-3}$ (equal to that of WC). The contact model of the particle was defined in terms of the four parameters $K_n$, $e$, $K_s$ and $\mu$. Liu et al. (2013) demonstrated that these parameters do not affect the interaction response of the granular assembly impacting the beam. However, we shall show via parametric studies that some of these contact properties strongly influence

the evolution of the granular slug as it emerges from the launcher. Unless otherwise specified, all calculations presented use the following set of parameters: $K_n = 1\,\mathrm{MNm^{-1}}$, $K_s/K_n = 2/7$ (Bathurst and Rothenburg, 1988; Silbert et al., 2001) and $e = \mu = 0.7$. Parameter studies to illustrate the sensitivity to these parameter choices are presented in Section 4.4.

## 4. Evolution of the granular slug during free-flight

It will be shown in Section 5 that an accurate prediction of the state of the granular slug just prior to its impact against the beam is critical in capturing the beam's dynamic deflection response. Thus, a key focus of this study is to predict the evolution of the granular slug as it is launched by the impact of the projectile.

Initial calculations suggested that three parameters dominated the evolution of the granular slug; viz. the inter-particle contact stiffness $K_n$, the piston velocity $v_p$ and the ramp time $T_R$ for the piston to acquire this velocity after impact by the projectile. We first discuss how the values of these parameters were selected, and then show the relatively weak dependence of the granular slug's evolution on the remaining contact parameters.

### 4.1 Estimation of the particle contact stiffness

Uth et al. (2015) measured the constrained compression of a WC particle slug in a cylindrical cavity as sketched in Fig. 8a. The dimensions and packing of the slug was identical to that used for impact experiments. The measured applied stress $\sigma_n$ (ratio of the applied compressive force to the cross-sectional area $A_0$ of the cylindrical cavity) versus nominal strain $\varepsilon_n$ (ratio the displacement of the piston to the initial height $h_0$ of the granular assembly within the cylinder) at a strain rate $\dot{\varepsilon}_n = 10^{-3}\,s^{-1}$ is plotted in Fig. 8b. This data was used to estimate the inter-particle stiffness $K_n$ used in the model.

The WC spherical particles were packed into a rigid cylindrical cavity as sketched in the inset in Fig. 8b to create a granular assembly of identical dimensions to that used in the experiment shown in Fig. 8a. The spherical particles had an initial volume fraction (prior to the application of the compressive force) of 0.57. Simulations of the compressive response were conducted by compressing the granular assembly via a rigid piston as shown in Fig. 8b at a displacement rate $\dot{\delta} = 200\,\mathrm{mm\,s^{-1}}$ (corresponding to a nominal strain rate $\dot{\varepsilon}_n = 10\,\mathrm{s^{-1}}$). The predicted nominal stress $\sigma_n$ versus nominal strain $\varepsilon_n$ responses are plotted (as three dashed lines) in Fig. 8b for three choices of $K_n$ with the remaining contact parameters kept fixed at their reference values. A contact stiffness $K_n = 1.0\,\mathrm{MN\,m^{-1}}$ brought the predictions into closest agreement with the measurements and this normal contact stiffness was then used as the reference case[6].

---

[6] The friction co-efficient, shear stiffness and damping do not affect the constrained compressive response shown in Fig. 8b over an applied strain rate range $1\,\mathrm{s^{-1}} \leq \dot{\varepsilon}_n \leq 100\,\mathrm{s^{-1}}$.
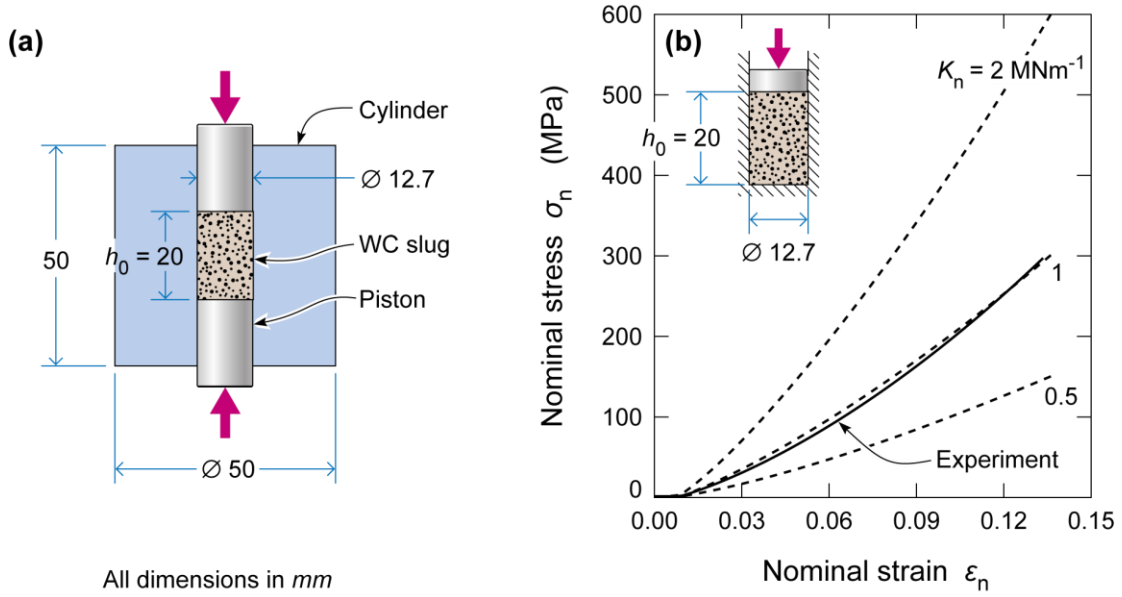
Figure 8: (a) Sketch of the experimental setup employed by Uth et al. (2015) to measure the constrained compression response of the granular slug. (b) Comparison between measurements (Uth et al., 2015) and predictions of the constrained compression response. Predictions are shown for three selected values of the normal inter-particle contact stiffness $K_n$ and the setup used in the simulations is shown as an inset.

## 4.2    The piston velocity

A magnified sketch of the impact of the projectile against the piston that pushes the slug out of the launcher is shown in Fig. 9a. Upon impact of the projectile both an elastic and plastic wave emanate from the impacted end and propagate towards the end of the piston in contact with the granular slug. These waves deform the piston and thus the end of the piston in contact with the slug does not attain its final velocity instantaneously. To illustrate this effect, we use the data of Uth et al. (2015) to plot the displacement in Fig. 9b of the four different markers on the piston shown in Fig. 9a for a projectile impact speed $V_0 = 217 \text{ m s}^{-1}$. These displacements in Fig. 9b are plotted as a function of time $t_I$, where $t_I = 0$ corresponds to the instant of impact of the projectile. The displacement rates of the markers (i.e. the marker velocities) all reach the constant and equal value at large $t_I$ as indicated in Fig. 9b. This is consistent with the fact that the deformation of the piston ceases at some time after impact of the projectile whereupon the piston behaves as a rigid body. This temporally and spatially constant marker velocity is defined as the piston velocity $v_p$: for the case of $V_0 = 217 \text{ m s}^{-1}$, $v_p = 83.5 \text{ m s}^{-1}$. The piston velocities for all the experiments of Uth et al. (2015) are analysed in this manner and the relation between $V_0$ and $v_p$ is shown in Fig. 9c. Thus, Fig. 9c provides the translation between data in Uth et al. (2015) presented in terms of $V_0$ and the numerical results presented here in terms of $v_p$.
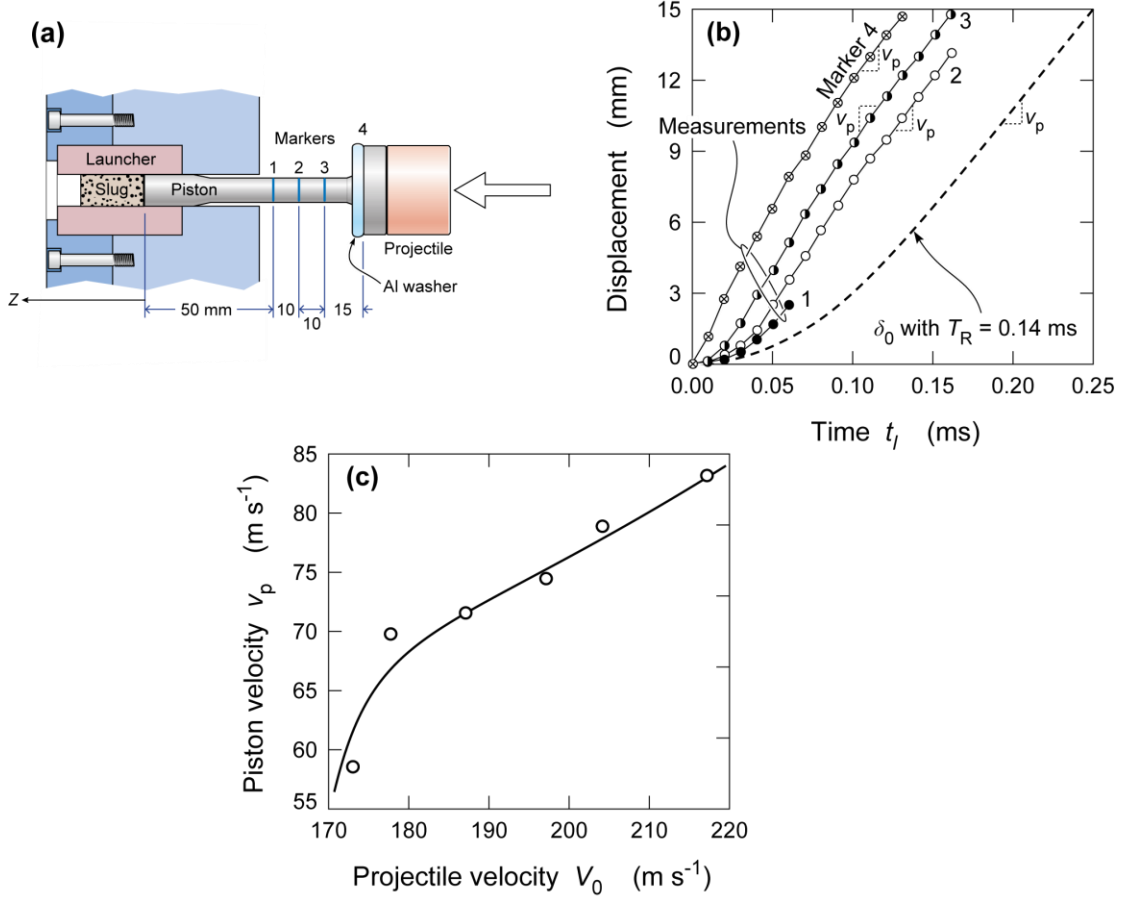
Figure 9: (a) Magnified view of the launcher with the granular slug and the piston that is just impacted by the projectile. The locations of four marker lines on the piston are shown whose displacements are followed from the high-speed photographs of Uth et al. (2015). (b) The temporal evolution of the displacements of the four marker lines in (a) for a projectile impact velocity $V_0 = 217 \text{ m s}^{-1}$. Here time $t_I = 0$ corresponds to the instant of impact of the projectile. (c) The relation between the piston velocity $v_p$ and projectile velocity $V_0$ inferred from the high-speed photographs of the piston motion.

### 4.3    The ramp time for piston to acquire its steady-state velocity

In order to simplify the numerical calculations, the piston is modelled as a rigid body, pushing the granular slug out of the launcher (Fig.4). The impact of the projectile with the piston is not directly modelled, but rather the loading is specified by prescribing the instantaneous velocity relation, $v_I(t_I)$ of the rigid piston. We thus need to prescribe to the rigid piston a $v_I(t_I)$ relation measured at the end of the deformable piston that is in contact with the granular slug. However, while this end was not visible in the experiments, the marker displacement data in Fig. 9b suggests a piecewise displacement versus time relation for all markers; viz. the displacements first increase approximately quadratically with time for small $t_I$ and then increase linearly with $t_I$. Thus, it is reasonable to approximate $v_I(t_I)$ as

$$
v_I = \begin{cases} \dfrac{v_p t_I}{T_R} & 0 \leq t_I \leq T_R \\ v_p & t_I > T_R, \end{cases} \tag{4.1}
$$

where $T_R$ is the time taken for the piston to ramp up to its final velocity $v_p$ after which it behaves as a rigid body. For an assumed value of $T_R = 0.14 \text{ ms}$, this gives a

temporal variation of the displacement $\delta_0 = \int v_I dt$ of the rigid piston as illustrated in Fig. 9b: we expect this displacement to closely resemble the displacement of the end of the piston in contact with the granular slug. While $T_R = 0.14$ ms seems a reasonable choice given the displacement data in Fig. 9b, we emphasize that $T_R$ cannot be directly inferred from the experimental measurements. We shall thus treat $T_R$ as a free parameter and estimate it by comparing measurements of metrics of the evolution of the slug with predictions.

Two key metrics of the measured evolution of the slug are used to calibrate $T_R$ and thereby judge the fidelity of the predictions:
(i) The velocity $v$ at six markers points along the slug. These markers are diametrical lines fixed at six equally spaced material points along the length of the slug when it first completely emerges from the launcher. This scheme is consistent with that employed by Uth et al. (2015) to characterise the particle velocities along the slug. The numbered markers are illustrated in the inset of Fig. 10a.
(ii) The evolution of the length $L_s$ of the slug with the distance $s$ travelled by the leading edge of the slug from its resting position as shown in Fig. 2c.

Simulations of the ejection of the granular slug from within the launcher were performed as follows. First the spherical WC particles were compacted into a cylindrical cavity of inner diameter $D_0 = 12.7$ mm capped at one end by a rigid piston as shown in Fig. 4a. The compacted slug had a length $L_0 = 20$ mm and the free end of the slug needed to travel a distance of 10 mm to emerge out of the launcher consistent with the experimental design of Uth et al. (2015). The piston was then imparted a velocity versus time history $v_I(t_I)$ using Eq. (4.1) so as to push the slug out of the launcher. Unless otherwise stated the results discussed here use the estimate, $T_R = 0.14$ ms.

Snapshots showing the predicted shape of the slugs at four values of $s$ for the $v_p = 83.5$ m s$^{-1}$ case are included in Fig. 2a along with the corresponding experimental observations. Consistent with the observations the simulations predict that the slug elongates with increasing $s$ while it's diameter remains largely unchanged. To quantify and explain this elongation of the granular slug, we proceed to characterise the velocity distribution along the length of the slug.

Predictions of the velocities of 3 selected markers for $v_p = 83.5$ m s$^{-1}$ are plotted in Fig. 10a as a function of $t_I$. Note that the markers were attached to material points after the slug first emerges from the launcher. Thus, these velocities were extracted from the simulations by tracing the velocities of material points associated with each marker over the entire time history from the instant of the projectile impact. After an initial transient, the material points along the markers acquire a temporally constant velocity. We denote these steady-state marker velocities as $v_{ss}$ and include predictions of $v_{ss}$ for the six different markers in Fig. 10b for two values of the piston velocity $v_p$. In both cases, $v_{ss}$ increases approximately linearly with marker number, i.e. the slug has a linear spatial velocity gradient with the leading edge moving faster compared to the trailing edge. Measurements of $v_{ss}$ from Uth et al. (2015) are included in Fig. 10b and show excellent agreement with the predictions for both the piston velocities. The velocity gradient along the slug implies that the slug elongates as it travels from the launcher towards its target. Predictions of the slug length $L_s$ as a function of the

distance travelled $s$ are included in Fig. 2c for two the values of $v_p$, and compare well with measurements over the entire range of measurements.
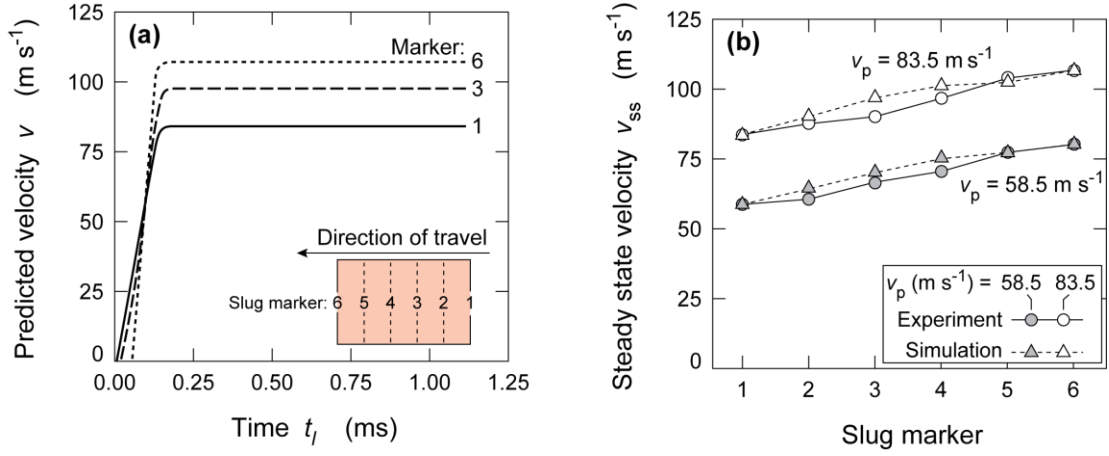


Figure 10: (a) Predictions of the temporal variation of the velocities of material points associated with selected marker lines on the granular slug generated by the piston at a velocity $v_p = 83.5 \text{ m s}^{-1}$. The slug is divided into 6 equal segments immediately after it completely emerges from the launcher as indicated in the inset. Time $t_I = 0$ corresponds to the instant of impact of the projectile. (b) Comparisons between predictions and measurements of the steady-state marker velocities $v_{ss}$ for two values of the piston velocity $v_p$. The simulations are shown with $T_R = 0.14$ ms.

The velocity gradient along the slug length implies that the packing density of particles evolves with $s$. To visualise the evolution of the spatial distribution of the slug density we define $\bar{n}$ as the number of particle per unit length of the slug in its current configuration. The density $\bar{n}$ is calculated by first dividing the slug at any instant into $\Delta L_s = 0.5$ mm long cylindrical discs and then defining $\bar{n}(z) \equiv N/\Delta L_s$, where $N$ is the number of particles within each disc centred at location with axial co-ordinate $z$. Predictions of $\bar{n}$ as function of a spatial co-ordinate $z$ are included in Fig. 11 at three selected times $t_I$ for $v_p = 83.5 \text{ m s}^{-1}$. Here, $z$ is defined in Fig. 9a as the spatial co-ordinate along the direction of travel of the slug with $z = 0$ corresponding to trailing edge of the slug at its resting position within the launcher. A linear spatial velocity gradient along the slug length would have implied a spatially uniform $\bar{n}$ along the slug with $\bar{n}$ decreasing with increasing $t_I$ as the slug elongates. However, the predictions in Fig. 11 clearly show a non-uniform spatial distribution of $\bar{n}$ illustrating that the spatial velocity gradient along the slug length is not completely linear with an accumulation of particles occurring towards the leading edge of the slug.
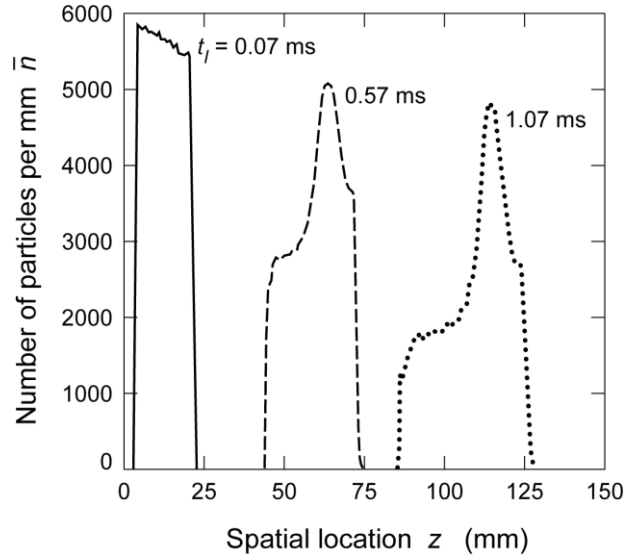
Figure 11: Predictions of the evolution of the number of particles per unit length $\bar{n}$ in the slug generated by the piston at a velocity $v_p = 83.5 \text{ m s}^{-1}$. The simulations are performed using $T_R = 0.14 \text{ ms}$ and the distribution $\bar{n}(z)$ shown at three selected times $t_I$, where $t_I = 0$ corresponds to the instant of impact of the projectile. The co-ordinate $z$ is defined in Fig. 9a.

The discussion above was restricted to $T_R = 0.14 \text{ ms}$ with good agreement between predictions and measurements obtained for all the measurements of Uth et al. (2015). To illustrate the sensitivity of the predictions to $T_R$ we include in Fig. 12 predictions of $v_{ss}$ for the six markers ($v_p = 83.5 \text{ m s}^{-1}$) for two additional values of $T_R$. It is clear that slightly higher or lower values of $T_R$ gives predictions of the spatial velocity gradients that are not in agreement with measurements. Given this agreement with the metrics of slug evolution and the displacement data of Fig. 9b, we argue that $T_R = 0.14 \text{ ms}$ is the appropriate value to use for simulating the experiments of Uth et al. (2015).
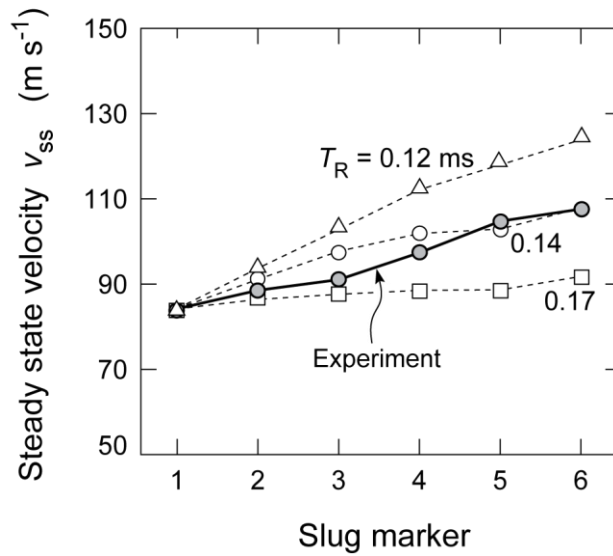


Figure 12: Comparisons between predictions and measurements of the steady-state marker velocities $v_{ss}$ of the slug for $v_p = 83.5 \text{ m s}^{-1}$ and three selected values of the ramp time $T_R$. All other parameters are kept fixed at their reference values.

16

*4.4    Sensitivity to contact model parameters*

We proceed to illustrate the sensitivity of the predictions of the evolution of the slug to the assumed inter-particle contact parameters with $T_R = 0.14$ ms. Predictions of the sensitivity of $v_{ss}$ for the six slug markers (at $v_p = 83.5$ m s$^{-1}$) to $K_n$, $e$ and $\mu$ are included in Figs. 13a, 13b and 13c, respectively. In each case the value of the parameter varied is indicated in the legend with all other contact parameters kept fixed at their reference values. The experimental measurements are included in each case for comparison purposes. It is clear that while the predictions are sensitive to $K_n$, the sensitivity to the co-efficient of restitution $e$ and friction co-efficient $\mu$ is negligible over a realistic ranges of these parameters. We emphasise that $K_n$ has been independently estimated using constrained compression test (Section 4.1) to justify the choice of $K_n = 1$ MN m$^{-1}$.
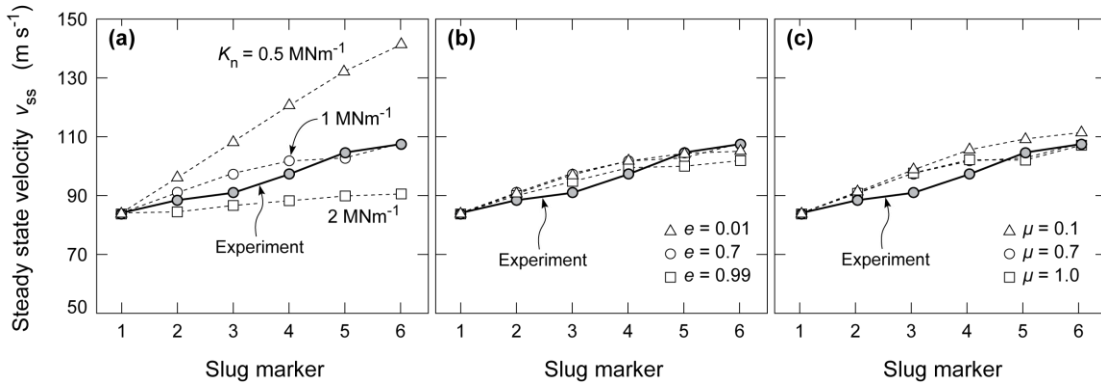


Figure 13: The sensitivity of the predictions of the steady-state marker velocities $v_{ss}$ of the slug for $v_p = 83.5$ m s$^{-1}$ to (a) the normal contact stiffness $K_n$, (b) co-efficient of restitution $e$ and (c) friction co-efficient $\mu$. In each case, predictions are shown for three values of the respective parameter with all other parameters kept fixed at their reference values. The experimental measurements (Uth et al., 2015) are included for comparison purposes in each case.

The predictions of Figs. 12 and 13 illustrate that the spatial velocity gradients increase with decreasing $T_R$ and $K_n$. This observation gives insight into the mechanism that results in the elongation of the granular slugs. The driving of the piston at $v_I(t_I)$ results in a compressive elastic wave propagating into the granular slug. When this compressive wave reaches the leading free-edge of the slug at time $T_L$, the entire slug starts to move. For times $t_I < T_L$, the displacement of the piston is accommodated solely by the compression of the slug. Thus, the compression of the slug is higher if (i) for a given $v_I(t_I)$, $T_L$ increases as the elastic wave speed is lower and (ii) for a given $T_L$, $T_R$ is reduced which then increases the piston displacement in time $T_L$. The elastic wave speed decreases with decreasing $K_n$ resulting in a larger compression and stored elastic energy within the slug. Similarly, the stored elastic energy increases with decreasing $T_R$. This stored elastic energy is released during the free-flight of the slug and results in a velocity gradient that causes the slug to elongate.

## 5.    Impact of granular slug against structures

To predict the response of clamped beams impacted normally and centrally by the granular slugs as reported by Uth et al. (2015), simulations were conducted as

described in Section 3.2 with the slug generated for any given piston velocity $v_p$ using the procedure discussed in Section 4. All simulations use the reference beam material and inter-particle contact properties listed in Section 3.3 and a ramp time $T_R = 0.14$ ms. Friction between the particles and beam surface was neglected.

*5.1    Impact against a clamped monolithic beam*
In the experiments of Uth et al. (2015), measurements are reported by varying two loading parameters; viz. the piston velocity $v_p$ and the stand-off $S$ defined as the distance between the leading end of the slug at its resting position within the launcher and the front end of the clamped beam; see Fig. 4. Predictions of both the influence of $v_p$ and $S$ on the observed response of the beams are therefore investigated.
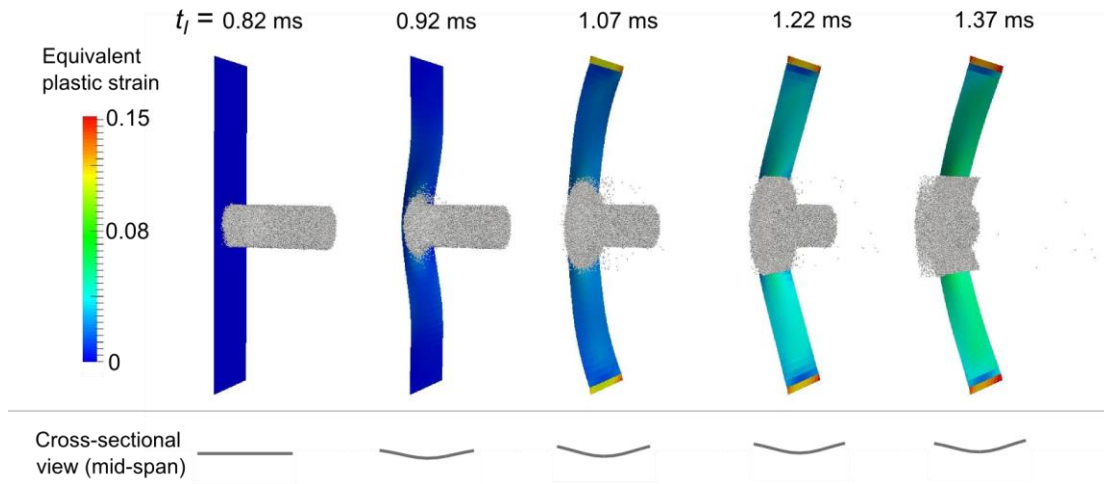


Figure 14: Predictions showing an angled view of the deformation of the beam and granular slug generated by a piston at $v_p = 69.5$ m s$^{-1}$ impacting the clamped beam at a stand-off $S = 65$ mm. Contours of von-Mises equivalent plastic strain are included on the beam and the snapshots shown at the 5 selected times $t_I$ used in Fig. 3. Here, time $t_I = 0$ corresponds to the instant the projectile impacts the piston. Cross sectional views of the mid-span of the beam are also shown for the each $t_I$.

Comparisons between predictions and observations of the deformation mode of the slug and the beam after impact by the slug are summarised in Fig. 3 for the case of $v_p = 69.5$ m s$^{-1}$ and $S = 65$ mm. Side view photographs showing the deformations from the experiments along with images of the same view from the simulations are included in Fig. 3 for 5 selected values of the time $t_I$. Consistent with the observations, the simulations predict that immediately after impact, a plastic wave emanates from the impact site and traverses towards the clamped end of the beam. Such dynamic plastic travelling hinges have been extensively reported; see for example Jones (1989). Simultaneously, the slug compacts and spreads against the beam. After the plastic hinges impinge upon the supports, the slug continues to compact against the beam and the beam deflection continues to increase by a stretching deformation mode. The beam reaches its maximum deflection at $t_I \approx 1.25$ ms. Some elastic rebound of the beam is observed both in the experiments and simulations after the peak deflection has been attained. This results in reflection of the granular particles in contact with the beam. An oblique view of the simulation snapshots shown in Fig. 3b is included in Fig. 14 with contours of the von Mises equivalent plastic strain now included for the beam. These images more clearly show

the spreading of the slug over the surface of the beam along both the width and beam length. Moreover, the contours illustrate that plastic strain (and probability of failure) is the maximized at the clamped supports, and although not visible in Fig.14, around the impact site. "Dishing" of the beam at the impact site was observed by Uth et al. (2015) and also predicted by the simulations as seen in the cross-sections of mid-span views included in Fig. 14.

Comparisons between the predictions and measurements of the variation of the mid-span deflections $w$ with time $t_I$ are included in Figs. 15a and 15b for $S = 65$ mm and 110 mm, respectively. Recall that the impact of the slug results in "dishing-type" deformation under the impact site and thus $w$ is measured both in the experiments and simulations at the geometric centre of the beam span. Excellent agreement for the temporal variation of $w$ is observed between the measurements and simulations. While the simulations proceed to long times where a permanent beam deflection is well defined, the temporal measurements of $w$ reported in Uth et al. (2015) do not span the full range of times simulated because spreading of the granular slug obscured the imaging of the beam deflection. However, we have included in Fig. 15 measurements of the permanent mid-span deflections $w_p$ reported in Uth et al. (2015) (measured with the beam still in the clamping rig but after all the elastic oscillations have damped out). The measured values of $w_p$ are in agreement with the steady-state values of the simulated beam deflections $w$.
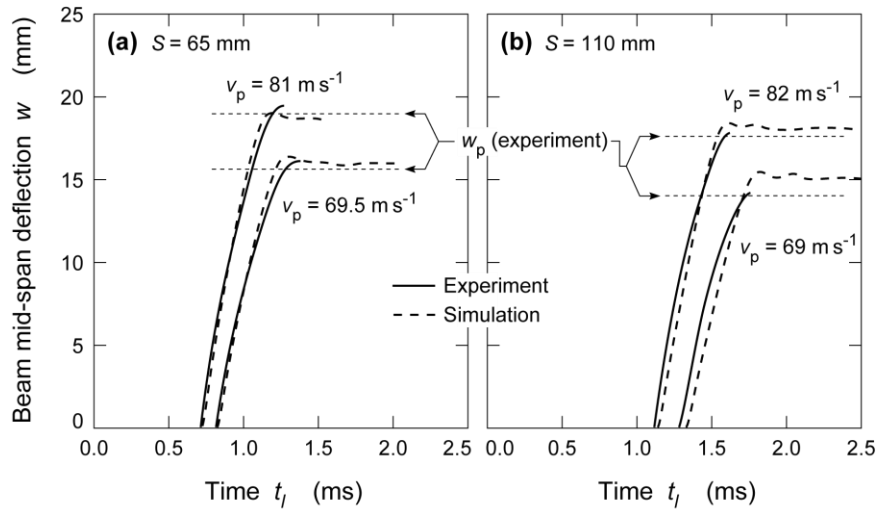


Figure 15: Predictions of the temporal variation of the deflection $w$ of the geometric centre of the clamped beam with time $t_I$ for a stand-off (a) $S = 65$ mm and (b) $S = 110$ mm. In each case, predictions are shown for two values of the piston velocity $v_p$ along with the corresponding experimental measurements of Uth et al. (2015). The permanent deflections $w_p$ reported by Uth et al. (2015) are indicated by horizontal dashed lines in each case. Time $t_I = 0$ corresponds to the instant the projectile impacts the piston.

Comparisons between predictions and measurements of $w_p$ over the range of piston velocities $v_p$ investigated by Uth et al. (2015) for two stand-off $S$ values are included in Fig. 5. The agreement over the entire range of measurements is always within 8% indicating the fidelity of the simulations. The increase in deflection with increasing $v_p$ is primarily due to the larger momentum of the impacting granular slug (i.e. the larger piston velocities impart a higher velocity to the granular slug). This larger momentum

results in larger beam deflections in line with simulations reported in a number of studies of granular impacts against deformable targets; see for example Liu et al. (2013), Dharmasena et al. (2013) and Wadley et al. (2013). However, the dependence of $w_p$ on slug stand-off is less clear since, for a given $v_p$, the momentum of the granular slug prior to impact against the beam is independent of $S$. We proceed to investigate this dependence by examining the impact of the slug against a rigid stationary target.

*5.2    Impact against a rigid stationary target*

Liu et al. (2013) demonstrated that the dynamic response of beams impacted by granular slugs with a spatially uniform density and velocity can be uniquely characterised in terms of two loading parameters: (i) a non-dimensional measure of the momentum of the slug and (ii) the ratio $\bar{\tau}$ of the loading time to the response time of the beam. A schematic representation of the predictions of Liu et al. (2013) are illustrated in Fig. 16 where the variation of the $w_p/L$ is plotted as a function of $\bar{\tau}$ for fixed values of the non-dimensional momentum $\bar{I}$. This sketch captures the salient points: (i) $w_p/L$ increases with $\bar{I}$ and (ii) for a given $\bar{I}$, $w_p/L$ increases with decreasing $\bar{\tau}$ until it reaches its maximum value corresponding to the impulsive limit for the given $\bar{I}$. As $S$ increases, the slug just prior to impact lengthens, resulting in a longer loading time (i.e. higher $\bar{\tau}$) and therefore smaller beam deflections. It is thus reasonable to conclude that the stand-off dependence seen here is due to slug elongation as it travels towards the beam.
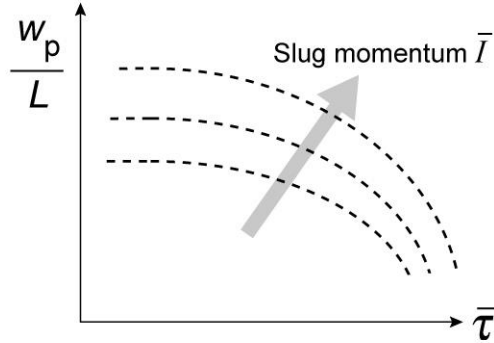


Figure 16: Sketch illustrating the dependence of the normalised beam deflections $w_p/L$ on the normalised loading time $\bar{\tau}$. Curves are shown for selected values of the normalised slug momentum $\bar{I}$. This sketch is inferred from the simulations of Liu et al. (2013) for slugs with spatially uniform density and velocities impacting clamped beams.

To investigate this further, simulations of the normal impact of the same granular slug against a rigid stationary wall have been conducted. These simulations can be used to determine the loading time and pressure history imparted by the granular slug as a function of the stand-off $S$ in the absence of any fluid-structure interaction effects that are operative during slug impact with a deformable beam. The setup used for the simulations was similar to that illustrated in Fig. 4 with one difference: the monolithic beam target was replaced by a rigid stationary wall. These calculations were conducted with contact properties between the particles and the wall identical to those between the deformable beam and the particles. Snapshots showing the deformation of the granular slug ($v_p \approx 69$ m s$^{-1}$) at four selected times $t_I$ are shown in Fig. 17 for

a rigid wall and a stand-off $S = 65$ mm. The slug compacts and spreads against the rigid target analogous to the spreading of a water jet during impingement on a rigid wall as previously reported by Pingle et al. (2012).
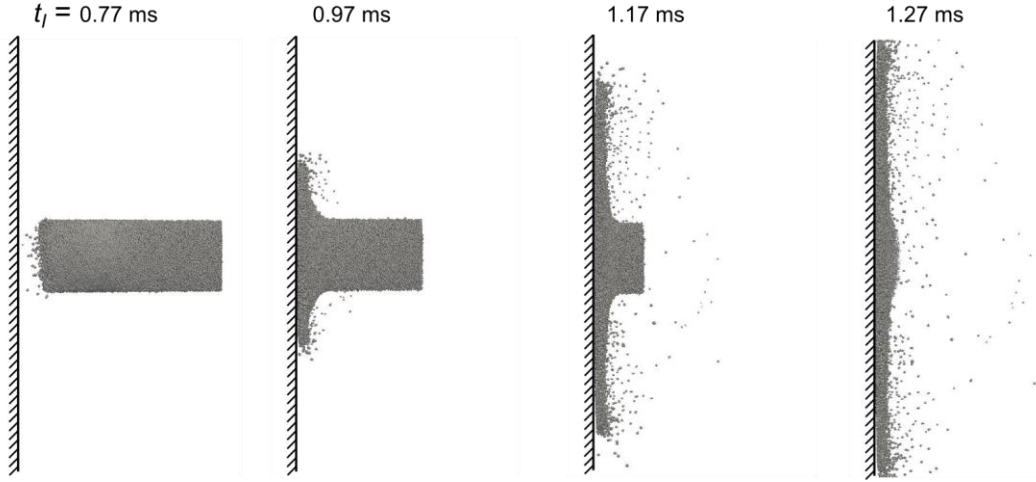


Figure 17: Predictions of the deformation of the slug generated by piston at $v_p \approx 69$ m s$^{-1}$ impinging the rigid wall at a stand-off $S = 65$ mm. Snapshots are shown at four selected times $t_I$, where $t_I = 0$ corresponds to the instant the projectile impacts the piston.
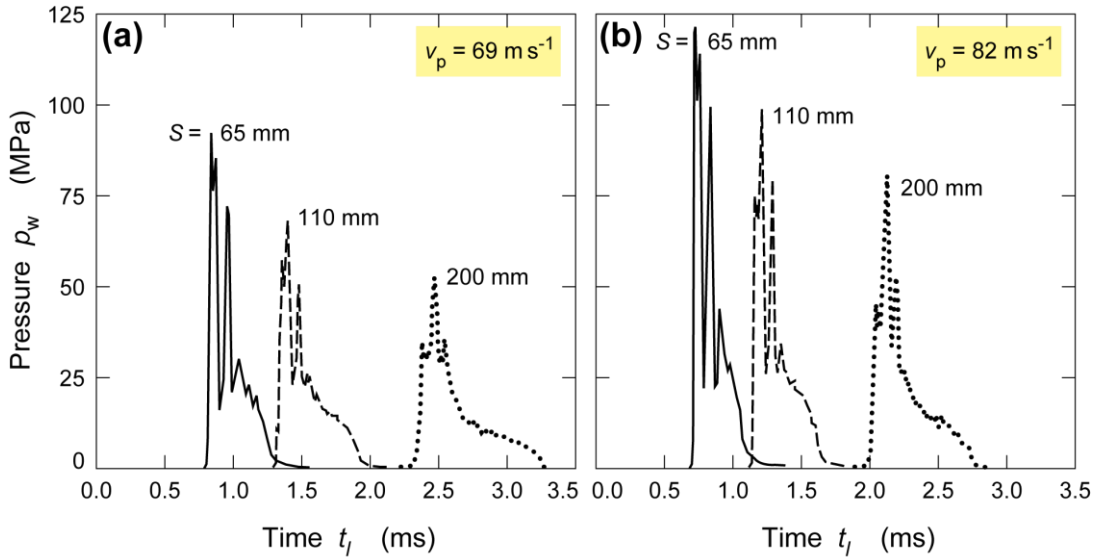


Figure 18: Predictions of the temporal variation of the pressure $p_w$ exerted by the granular slug impinging normally on a rigid stationary target. The slugs are generated by piston velocities (a) $v_p = 69$ m s$^{-1}$ and (b) $v_p = 82$ m s$^{-1}$. Results are shown in each case for three values of the stand-off $S$ with time $t_I = 0$ corresponding to the instant the projectile impacts the piston.

We define a nominal pressure $p_w(t_I)$ exerted by the impinging slug on the wall as the ratio of the total force $F_w(t_I)$ exerted by the particles on the wall at time $t_I$ and the cross-section area $\pi D_0^2/4$ of the slug within the launcher. Predictions of the variation of $p_w$ with $t_I$ are included in Figs. 18a and 18b for piston velocities $v_p = 69$ m s$^{-1}$ and 82 m s$^{-1}$, respectively and three values of the stand-off $S$ in each case. In all the cases, there is a sudden rise in the contact pressure $p_w$ immediately upon the impact

of the slug and subsequently the general trend is for the pressure to decrease. This decrease can be rationalised by noting that we expect the scaling the pressure to follow $p_w \propto \rho v^2$ (Park et al., 2013) where $\rho$ and $v$ are the density and velocity of the region of the slug currently in contact with the wall. The decrease in $p_w$ with increasing time is consistent with the fact that the particle velocity $v$ decreases from the leading to the trailing edge of the slug; see Fig. 10b. The slug elongates as it travels further and thus the loading time increases with increasing $S$. Since the total slug momentum is independent of $S$, the average contact pressure therefore decreases with increasing $S$.

The predictions of the contact pressure exerted by the slug upon normal impact against a rigid stationary target clearly show that the contact pressures decrease with increasing $S$ and decreasing $v_p$. This results in the stand-off and piston velocity dependencies of the beam deflections seen in Fig. 5. For the sake of completeness we have included predictions of the permanent deflections of the beam as a function of $v_p$ in Fig. 5 for a stand-off $S = 200$ mm (Uth et al. (2015) did not report measurements for this case). Consistent with expectations, the beam deflections are lower compared to the $S = 65$ mm and 110 mm cases.

## 6.      Concluding remarks

Coupled discrete particle/continuum simulations for the normal impact of granular slugs against deformable clamped beams have been reported. The simulations were designed to replicate the experimental setup employed by Uth et al. (2015) and detailed comparisons have been made with those observations.

A high velocity granular slug of cylindrical geometry is generated by the ejection of the slug from a launcher by the pushing action of a piston. The pushing action results in storage of elastic strain energy within the slug. The release of this elastic energy during free-flight results in axial stretching due to spatial velocity gradients within the slug. These velocity gradients are a strong function of the inter-particle contact stiffness and the time required for the piston to reach its final velocity. Other inter-particle contact properties such as damping and friction have a negligible effect on the evolution of the granular slug as it was launched towards its target. Experimental observations were used to estimate both the effective contact stiffness and the piston ramp time. Numerical predictions using these values were in agreement with observations for the evolution of the granular slug in terms of the spatial velocity gradients as well as the overall length of the slug.

Coupled finite element/discrete particle simulations of the impact of these slugs against clamped beams enabled the temporal evolution of the deformations as well as the permanent deflections of the beams to be predicted and compared with measurements. The predictions agreed well with the observations. The increase in the deflections with the slug velocity was a direct consequence of the higher momentum of the slug. The stand-off dependence arose from the lengthening of the slugs as they travel towards the beams. This lengthening resulted in longer loading times and lower contact pressures on the beams which resulted in smaller permanent (plastic) deflections.

The studies of Liu et al. (2013) and Pingle et al. (2012) demonstrated that for a given sand slug (i.e. given spatial velocity and density distribution), the response of

structures is relatively insensitive to the contact properties of the granular particles. However, here we demonstrate that the generation of the slug due to shock loading applied via a piston strongly depends on at-least the time required to accelerate the granular media and the normal contact stiffness between the particles. The ensuing velocity and density distributions within the slug in turn govern the responses of the impacted beams and results in a stand-off effect. There is a wealth of experimental data that suggests a strong dependence of the effect of the type of granular media and stand-off on the response of structures subjected to landmine loading (Fourney et al., 2005; Pickering et al., 2012; Holloman et al., 2015a, 2015b). The simulations reported here have shed light into mechanisms that may help rationalise such observations.

**References**

Anderson, C.E., Behner, T., Holmquist, T.J., Orphal, D.L., 2011. Penetration response of silicon carbide as a function of impact velocity. Int. J. Impact Eng. 38, 892–899. doi:10.1016/j.ijimpeng.2011.06.002

Bathurst, R.J., Rothenburg, L., 1988. Micromechanical aspects of isotropic granular assemblies with linear contact interactions. J. Appl. Mech. 55, 17–23.

Bergeron, D., Tremblay, J.E., 2000. Canadian research to characterize mine blast output. Proc. 16th Int. MABS Symp. Oxford, UK.

Borvik, T., Olovsson, L., Hanssen, A.G., Dharmasena, K.P., Hansson, H., Wadley, H.N.G., 2011. A discrete particle approach to simulate the combined effect of blast and sand impact loading of steel plates. J. Mech. Phys. Solids 59, 940–958. doi:10.1016/j.jmps.2011.03.004

Campbell, C.S., 2002. Granular shear flows at the elastic limit. J. Fluid Mech. 465, 261–291. doi:10.1017/S002211200200109X

Campbell, C.S., Brennen, C.E., 1985. Chute flows of granular material: Some computer simulations. J. Appl. Mech.

Cundall, P.A., Strack, O.D.L., 1979. A discrete numerical model for granular assemblies. Géotechnique 29, 47–65. doi:10.1680/geot.1979.29.1.47

Deshpande, V.S., Fleck, N.A., 2005. One-dimensional response of sandwich plates to underwater shock loading. J. Mech. Phys. Solids 53, 2347–2383. doi:10.1016/j.jmps.2005.06.006

Deshpande, V.S., McMeeking, R.M., Wadley, H.N.G., Evans, A.G., 2009. Constitutive model for predicting dynamic interactions between soil ejecta and structural panels. J. Mech. Phys. Solids 57, 1139–1164. doi:10.1016/j.jmps.2009.05.001

Dharmasena, K.P., Queheillalt, D.T., Wadley, H.N.G., Dudt, P., Chen, Y., Knight, D., Evans, a. G., Deshpande, V.S., 2010. Dynamic compression of metallic sandwich structures during planar impulsive loading in water. Eur. J. Mech. A/Solids 29, 56–67. doi:10.1016/j.euromechsol.2009.05.003

Dharmasena, K.P., Wadley, H.N.G., Liu, T., Deshpande, V.S., 2013. The dynamic response of edge clamped plates loaded by spherically expanding sand shells. Int. J. Impact Eng. 62, 182–195. doi:10.1016/j.ijimpeng.2013.06.012

Fairlie, G., Bergeron, D., 2002. Numerical Simulation of Mine Blast Loading on Structures. 17th Mil. Asp. Blast Symp. Las Vegas, Nevada 2–9.

Foedinger, J., 2005. Methodology for improved characterization of landmine explosions, SBIR Phase-II plus program. 2005. Proc. Tech. Interchang. Meet. Mater. Sci. Corp.

Fourney, W., Leiste, U., Bonenberger, R., Goodings, D., 2005. Explosive impulse on plates. Fragblast 9, 1–17.

Grujicic, M., Pandurangan, B., Cheeseman, B.A., 2006. The effect of degree of saturation of sand on detonation phenomena associated with shallow-buried and ground-laid mines. Shock Vib. 13, 41–61.

Grujicic, M., Pandurangan, B., Mocko, G.M., Hung, S.T., Cheeseman, B. a., Roy, W.N., Skaggs, R.R., 2008a. A Combined Multi-Material Euler/Lagrange Computational Analysis of Blast Loading Resulting from Detonation of Buried Landmines. Multidiscip. Model. Mater. Struct. 4, 105–124. doi:10.1163/157361108784050086

Grujicic, M., Pandurangan, B., Qiao, R., Cheeseman, B.A., Roy, W.N., Skaggs, R.R., Gupta, R., 2008b. Parameterization of the porous-material model for sand with different levels of water saturation. Soil Dyn. Earthq. Eng. 28, 20–35. doi:10.1016/j.soildyn.2007.05.001

Hlady, S., 2004. Effect of soil parameters on landmine blast. 18th Mil. Asp. Blast Shock Conf. Bad Reichenhall, Ger.

Holloman, R.L., Deshpande, V.S., Wadley, H.N.G., 2015a. Impulse transfer during sand impact with a solid block. Int. J. Impact Eng. 76, 98–117. doi:10.1016/j.ijimpeng.2014.09.010

Holloman, R.L., Deshpande, V.S., Wadley, H.N.G., 2015b. Impulse transfer during sand impact with a cellular structure. Int. J. Impact Eng. doi:10.1016/j.ijimpeng.2015.01.004

Jones, N., 1989. Structural impact. Cambridge Univ. Press. Cambridge, UK. doi:10.1017/CBO9781107415324.004

Lichtenfeld, J.A., Mataya, M.C., Tyne, C.J.V., 2006. Effect of strain rate on stress-strain behavior of alloy 309 and 304L austenitic stainless steel. Metall. Mater. Trans. A 37, 147–161.

Liu, T., Fleck, N.A., Wadley, H.N.G., Deshpande, V.S., 2013. The impact of sand slugs against beams and plates: Coupled discrete particle/finite element simulations. J. Mech. Phys. Solids 61, 1798–1821. doi:10.1016/j.jmps.2013.03.008

Morris, B.L., 1993. Analysis of improved crew survivability in light vehicles subjected to mine blast. Final Rep. Contract no. DAAK70-92-C-0058 U.S. Army Belvoir RDEC, Ft. Belvoir, VA.

Neuberger, A., Peles, S., Rittel, D., 2007. Scaling the response of circular plates subjected to large and close-range spherical explosions. Part II: Buried charges. Int. J. Impact Eng. 34, 874–882. doi:10.1016/j.ijimpeng.2006.04.002

Park, S., Uth, T., Fleck, N.A., Wadley, H.N.G., Deshpande, V.S., 2013. Sand column impact onto a Kolsky pressure bar. Int. J. Impact Eng. 62, 229–242. doi:10.1016/j.ijimpeng.2013.07.003

Peles, S., Touati, D., Azulay, I., Neuberger, A., 2008. Numerical simulation of mine detonation beneath a generalized add-on armor structure. Proc. 24th Int. Symp. Ballist. 1. Lancaster, PA DEStech Publ. Inc. 439–47.

Pickering, E.G., Chung Kim Yuen, S., Nurick, G.N., Haw, P., 2012. The response of quadrangular plates to buried charges. Int. J. Impact Eng. 49, 103–114. doi:10.1016/j.ijimpeng.2012.05.007

Pingle, S.M., Fleck, N.A., Wadley, H.N.G., Deshpande, V.S., 2012. Discrete element calculations of the impact of a sand column against rigid structures. Int. J. Impact Eng. 45, 74–89. doi:10.1016/j.ijimpeng.2011.10.005

Plimpton, S., 1995. Fast parallel algorithms for short range molecular dynamics. J. Comput. Phys. 117, 1–19.

Reichenbach, H., Behrens, K., Kuhl, A.L., 1991. Exploratory depth-of-burst experiments. Interim report, Contract No. DNA 001-91-C-0039, Prep. Def. Nucl. Agency, Washington, DC, USA. doi:10.1017/CBO9781107415324.004

Rimoli, J.J., Talamini, B., Wetzel, J.J., Dharmasena, K.P., Radovitzky, R., Wadley, H.N.G., 2011. Wet-sand impulse loading of metallic plates and corrugated core sandwich panels. Int. J. Impact Eng. 38, 837–848. doi:10.1016/j.ijimpeng.2011.05.010

Silbert, L., Ertas, D., Grest, G., Halsey, T., Levine, D., Plimpton, S., 2001. Granular flow down an inclined plane: Bagnold scaling and rheology. Phys. Rev. E 64, 051302. doi:10.1103/PhysRevE.64.051302

Taylor, G.I., 1963. The pressure and impulse of submarine explosion waves on plates. The Scientific Papers of Sir Geoffrey Ingram Taylor. Aerodyn. Mech. Proj. Explos. G. Batchelor, Cambridge Univ. Press. Cambridge, UK Vol. III, 287–303.

Uth, T., Deshpande, V.S., 2014. Response of clamped sandwich beams subjected to high-velocity impact by sand slugs. Int. J. Impact Eng. 69, 165–181. doi:10.1016/j.ijimpeng.2014.02.012

Uth, T., Wadley, H.N.G., Deshpande, V.S., 2015. The effect of inclination and stand-off on the dynamic response of beams impacted by slugs of a granular material. Int. J. Solids Struct. 56-57, 154–174. doi:10.1016/j.ijsolstr.2014.11.019

Wadley, H.N.G., Børvik, T., Olovsson, L., Wetzel, J.J., Dharmasena, K.P., Hopperstad, O.S., Deshpande, V.S., Hutchinson, J.W., 2013. Deformation and fracture of impulsively loaded sandwich panels. J. Mech. Phys. Solids 61, 674–699. doi:10.1016/j.jmps.2012.07.007

Wadley, H.N.G., Dharmasena, K., Chen, Y., Dudt, P., Knight, D., Charette, R., Kiddy, K., 2008. Compressive response of multilayered pyramidal lattices during underwater shock loading. Int. J. Impact Eng. 35, 1102–1114. doi:10.1016/j.ijimpeng.2007.06.009

Wang, Z., Hao, H., Lu, Y., 2004. A three-phase soil model for simulating stress wave propagation due to blast loading. Int. J. Numer. Anal. Methods Geomech. 28, 33–56. doi:10.1002/nag.325

Wei, Z., Dharmasena, K.P., Wadley, H.N.G., Evans, a. G., 2007. Analysis and interpretation of a test for characterizing the response of sandwich panels to water blast. Int. J. Impact Eng. 34, 1602–1618. doi:10.1016/j.ijimpeng.2006.09.091

Westine, P.S., Morris, B.L., Cox, P.A., Polch, E., 1985. Development of computer program for floor plate response from land mine explosions. Contract Rep. No. 1345 U.S. Army TACOM Res. Dev. Cent.